

Wolf–Rayet stars in M 81 using GTC/OSIRIS: 7 new detections, analysis and classification of the full sample

V. M. A. Gómez-González^{1,2,3*}, Y. D. Mayya¹, D. Rosa-González¹,
L. H. Rodríguez-Merino¹, J. A. Toalá³ and C. Alvarez²

¹*Instituto Nacional de Astrofísica, Óptica y Electrónica, Luis Enrique Erro 1, Tonantzintla 72840, Puebla, Mexico*

²*Universidad Autónoma de Chiapas, Blvd. Belisario Domínguez, Km. 1081, Terán Tuxtla Gutiérrez 29050, Chiapas, Mexico*

³*Instituto de Radioastronomía y Astrofísica, UNAM Campus Morelia, Apartado postal 3-72, 58090 Morelia, Michoacan, Mexico*

10 February 2020

ABSTRACT

We report the detection of 7 new Wolf-Rayet (WR) star locations in M 81 using the Multi-Object Spectrograph of the OSIRIS instrument at Gran Telescopio Canarias. These detections are the result of a follow-up of an earlier study using the same instrumental set-up that resulted in the detection of 14 WR locations. We analyse the entire sample of 21 spectra to classify them to one of the known WR sub-types using template spectra of WR stars in the Large Magellanic Cloud (LMC), with similar metallicity to M 81. Taking into consideration the dispersion in the strengths of the bumps for a given WR sub-type, we found that 19 of the 21 locations correspond to individual stars, including all the 7 new detections, of sub-types: WNL, WNE, WCE and the transitional WN/C. None of the detections correspond to WCL or WO types. The positions of these stars in the red bump vs blue bump luminosity diagram agrees well with an evolutionary path according to the Conti scenario. Based on this, we propose this diagram as a straightforward tool for spectral classification of extragalactic WR sources. The detection of individual WR stars in M 81, which is at a distance of 3.6 Mpc, opens up a new environment for testing the massive star evolutionary models.

Key words: stars: emission-line – stars: evolution — stars: massive — stars: Wolf-Rayet — galaxies: individual (M 81)

1 INTRODUCTION

Wolf-Rayet (WR) stars are related to some of the most exotic and interesting astronomical objects in the Universe, e.g. the most massive stars, binaries, supernova (SN) explosions, compact objects (neutron stars and black holes), Gamma Ray Bursts (GRBs) and gravitational waves. Theoretical models predict that WR stars will end their lives as powerful core collapse SNIbc, and recent observational works suggest that rotating WR stars might be also involved in the production of GRBs (see Vink et al. 2011, and references therein). Assuming an average WR lifetime: $t_{\text{WR}} \sim 0.4$ Myr, Moffat (2015) uses the equation $T = t_{\text{WR}}/2N$ to estimate that a random sample of $N \sim 1000$ WR stars is needed in order to expect a SN explosion in the next 200 yrs ($N \sim 10^5$ for $T = 2$ yrs). The greater the number of WR stars found,

the greater the probability of detecting one of these explosive events in a reasonable human life-time. However, not a single SN, nor a GRB event, has been directly traced back to a previously classified WR star (~ 150 yrs have passed since their discovery). Moreover, a detailed characterization of individual WR stars is mandatory to establish a direct connection with theoretical predictions in massive star evolution and feedback (Meynet & Maeder 2005; Chen et al. 2015; Eldridge et al. 2017).

Extragalactic searches help to increase the WR sample. The advent of multiple object spectroscopy (MOS) in large telescopes has facilitated spectroscopic confirmation of large samples of WR star candidates in nearby galaxies, e.g. M 31 (0.76 Mpc; Neugent et al. 2012), M 33 (0.84 Mpc; Neugent & Massey 2011), NGC 300 (2 Mpc; Schild et al. 2003) and NGC 1313 (4.1 Mpc; Hadfield & Crowther 2007). It is important to note that in galaxies that are further away, the studies of individual WR stars are scarce.

* E-mail: v.gomez@irya.unam.mx

In Gómez-González et al. (2016) (hereafter Paper I), we reported the first results of an observational program for the detection of WR stars in M 81. Our spectroscopic targets were blue knots in star forming regions in the spiral arms, selected in archival *Hubble Space Telescope* (*HST*) images. We reported the detection of the first population of WR stars in M 81, a grand design spiral galaxy at the relatively close distance of 3.63 Mpc ($m - M = 27.8$; Freedman et al. 1994), using longslit and MOS modes of OSIRIS spectrograph at the 10.4-m Gran Telescopio Canarias (GTC). The bump strengths in 12 of our 14 detections were consistent with those from individual WR stars, comprising of WNL, WNE, WCE and transitional WN/C sub-types, as inferred using the templates for the Large Magellanic Cloud (LMC) WR stars. With the exception of two, all our WR locations were surrounded by ionized bubbles. The presence of ionized bubbles around WR stars are expected since they are hot stars supplying both ionizing photons and high velocity winds, in addition to being situated in a gaseous environment, favouring the creation of ionized bubbles. Hence we targeted the central stars of a large sample of ionized bubbles for a follow-up spectroscopic search for WRs with GTC.

In this paper, we present the detection of new locations with WR features and a homogeneous analysis of the full sample, dereddened for dust extinction. In Paper I, we analysed our spectra using templates from WR stars in the LMC, described in Crowther & Hadfield (2006) and publicly available in the website of P.Crowther. Recent analysis of chemical abundances in M 81 suggest a uniform abundance in most parts of its disk (Arellano-Córdova et al. 2016). In particular, at galacto-centric distances of $0.35\text{--}0.6 R_{25}$, where our WR stars are located, direct method gives $12 + \log(\text{O}/\text{H})=8.10$, which is closer to that of the LMC than that of our Galaxy. LMC templates are appropriate to analyse the WR features in M 81 since it also has examples of WNL, WNE and WCE subtypes. We also explore a multi-component Gaussian fitting of the broad WR bumps into individual ionic transitions, in order to construct a red bump (RB) vs blue bump (BB) luminosity diagram.

This paper is structured as follows: candidate sample of ionized bubbles, spectroscopic observations, reduction, WR identification, extraction and new sample are presented in §2; template fitting of M 81 spectra using LMC templates are presented in §3; diagnostic diagrams are presented in §4. Finally, summary and concluding remarks are presented in §5.

2 OBSERVATIONS

2.1 Sample of central stars of ionized bubbles

Motivated by the success of detecting individual WR stars through GTC/OSIRIS spectroscopic observations in M 81, we carried out follow-up observations of a carefully selected candidate sample with the goal of increasing the number of individual WR stars. Our previous 14 detections reported in Paper I were serendipitous and were located in slits passing through *HST*-selected blue knots in star-forming regions. Given that 12 of the 14 detected WR stars were associated with ionised bubbles, we targeted the central stars of ionised bubbles for these new observations. Bubble-like

Table 1. Details of our GTC/OSIRIS MOS spectroscopic observations[†] in M 81.

Pointing	Date	Exposure Time (s)	Air mass	Seeing (")
MOS1	2015-03-16T22:11:03	3×923	1.33	0.8
MOS2	2015-03-14T22:33:47	3×923	1.32	0.9
MOS3	2015-03-15T22:32:37	3×923	1.32	1.0

[†]These observations were part of the proposal GTC7-15AMEX (PI: Gómez-González). The location of the 3 pointings are shown in Fig. 1. The date column also gives the starting Universal Time of the 1st of the 3 frames, taken one after another.

structures are expected around WR stars: massive O-type stars evolve into red supergiant or luminous blue variable stars and lose mass through dense and slow winds to become WR stars. The strong UV flux from WR stars ionize the ejected material, giving rise to shells usually detected through H α narrow-band images (e.g. Chu et al. 1983; Gruendl et al. 2000). Furthermore, these shells are expected to be swept away by the fast winds from the WR stars forming the so-called ring nebulae or WR nebulae (García-Segura et al. 1996; Toalá & Arthur 2011). The sizes of bubbles in coeval stellar cluster can reach several tens of parsecs, such as those observed around our reported WR detections in M 81 (see Fig. 1 in Paper I).

In order to select a sample of candidates for spectroscopic follow-up, we carried out a systematic visual search for ionized bubbles in M 81 using archival *HST* images. The *HST* has observed M 81 with the Advanced Camera for Surveys (ACS), with the F435W, F606W and F814W broadband filters covering the full optical extent of this galaxy. In particular, we looked for extended structures that are visible only in the F606W filter. The H α emission line intercepts this filter, which allows to trace the ionized structures such as bubbles at a spatial resolution of $0.1''$ (1.8 pc). A systematic search resulted in a catalogue of ~ 300 bubbles with a median radius of ~ 12 pc. Around a third of these bubbles contained a bright blue star within its boundaries. This star is most likely to be either an individual O-star or a WR star, and hence we considered it as a primary candidate for positioning the MOS slitlets. We note that, since the majority of Galactic WR stars are not necessarily coincident with star-forming regions (e.g. Rosslowe & Crowther 2015), we do not anticipate completeness of the WR population through our spectroscopic study of M 81.

2.2 Spectroscopic Observations

Spectroscopic observations of the candidate central stars of bubbles were carried out using the OSIRIS instrument in its MOS mode at the 10.4-m GTC (Cabrera-Lavers 2016). Table 1 gives the details of these observations. Three MOS pointings were used and their locations are shown in Figure 1. Each MOS field of view (FoV) of $\sim 7.4' \times 2.0'$ included $\sim 80\text{--}90$ slitlets of varying lengths, including $\sim 5\text{--}6$ stars as fiducial points for astrometry. When possible, the slitlets contained object-free regions for background subtraction. Additionally, we placed around a dozen slitlets for the purpose of accurate sky/background determination. Given

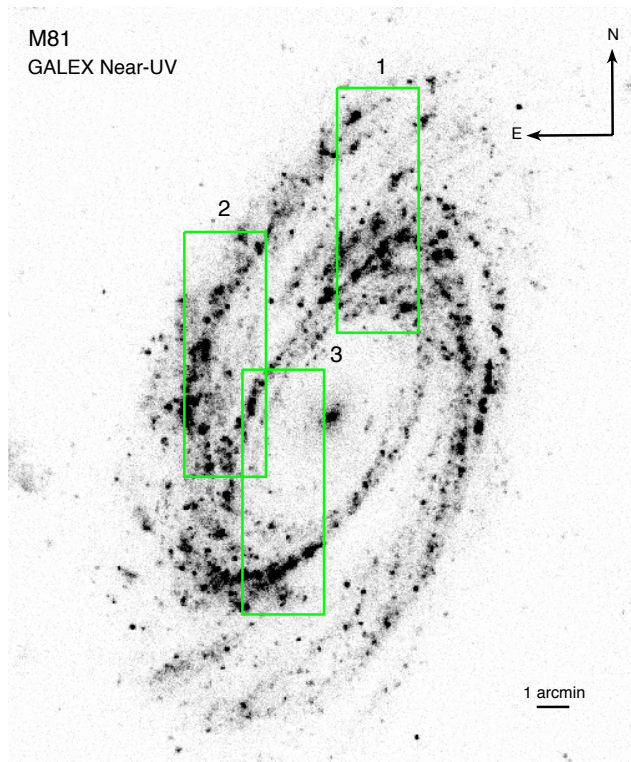


Figure 1. *GALEX* near-UV image of M81 showing the location of the 3 GTC/OSIRIS-MOS fields (green rectangles of $\sim 7.4' \times 2.0'$) analysed in the present work. Each FoV contained ~ 80 – 90 slitlets of $1.2''$ width of varying lengths placed on the central stars of ionized bubbles.

the geometrical restrictions of mask designer, we could place slitlets on ~ 180 central stars of bubbles, our most likely WR candidates.

We used the same spectroscopic setting as in our earlier observations presented in Paper I, i.e., the R1000B grism, slitwidth of $1.2''$, spectral range of ~ 3700 to 7500 \AA , spectral resolution of $\sim 7 \text{ \AA}$ and a CCD binning of 2×2 . The observations have a spatial scale of $0.254'' \text{ pixel}^{-1}$ and spectral sampling of $\sim 2 \text{ \AA pixel}^{-1}$. The observations were carried out in service mode, with the total observing time split into blocks of ~ 60 min, each corresponding to a particular MOS pointing, and consisted of 3 exposures of equal integration time to facilitate later removal of cosmic rays. Data from each block contained auxiliary files that included standard stars, bias, flat-field and arc lamps. The sky was stable during all the observations with a seeing between 0.8 – $1.0''$.

2.3 Reductions, WR identification and extraction

The procedure adopted for the reduction and extraction of spectroscopic data is similar to that described in Paper I. Reduction was carried out using the package GTCMOS, a tailor-made IRAF-based pipeline¹ developed by Y. D. Mayya for the reduction of the OSIRIS spectra. Wavelength and

flux-calibrated 2-D spectral images of the 3 fields are visually examined on a display monitor for the identification of the blue bump, a characteristic signature of a WR star. Out of the 179 spectra of central stars, we identified 7 spectra containing WR features. The remaining objects are mostly O and early B-stars, which will be the subject of study in a future work.

The physical scale of the slitwidth (~ 21 pc, at the distance of M81) is large enough to include more than one star. However, our targets were pre-selected to contain a stellar object in the slit at the *HST* resolution of (~ 1.8 pc). This allowed easy association of a spectra with a detected WR feature to a star on the *HST* image. In Figure 2, we show colour-composite *HST* ACS images of the 7 new detections.

Bumps of WR 15, WR 17, WR 18 and WR 20 had an associated continuum. For each of these WR features, an 1-D spectrum was extracted using the IRAF task *apall*, summing spectra over 4–7 pixel, depending on each case, about the traced continuum. On the other hand, WR 16, WR 19 and WR 21 did not have an associated continuum. In these cases, the continuum of a bright object, close enough to each continuum-less WR, was used as a reference. The *reference* parameter from task *apall* was activated to use the polynomial of the continuum as reference for extraction.

2.4 The updated sample of WR stars in M81

The 7 new WR detections, labelled as WR 15–WR 21, along with the previous 14 objects reported in Paper I, add up to a total of 21 WR detections in M81. Table 2 lists some of their basic parameters, where the first 14 entries are taken from Paper I. The photometry for the new sources was carried out using IRAF task *phot* as in Paper I. We also list the size of the nebulosity around the WR object, when present, as measured on the *HST* F606W image, and the name of the star-forming complex, from Pérez-González et al. (2006), embedding the WR location. The locations of these 21 WR sources are indicated in Figure 3, which is a colour-composite wide-field *HST* ACS mosaic image. As expected, all the WR sources are confined to the spiral arms, which is hosting many star forming regions.

Individual stars and nebulae in M81 are known to suffer a mean extinction of $A_V \sim 0.8$ (e.g. Kudritzki et al. 2012; Humphreys et al. 2019) which is much higher than $A_V(\text{Gal}) = 0.20$ along the line of sight to M81. Thus, the observed spectra need to be corrected for reddening. For this purpose, we determined the visual extinction $A_V(\text{nebula})$ using the Balmer decrement method. We measured the $H\alpha$ and $H\beta$ emission line fluxes in each extracted WR spectrum and obtained $A_V(\text{nebula})$ assuming intrinsic Balmer decrement ratio corresponding to a case B photoionized nebula of $T_e = 10000 \text{ K}$ and $n_e = 100 \text{ cm}^{-3}$ (Osterbrock & Ferland 2006) and the reddening curve of Cardelli et al. (1989). The resulting $A_V(\text{nebula})$ are listed in the last column of Table 2. In five cases (WR6, WR9, WR11, WR15 and WR20), A_V obtained from Balmer decrement was of the same order or marginally less than $A_V(\text{Gal}) = 0.20$, in which case, we report $A_V(\text{Gal}) = 0.20$ in this column. In two other cases (WR2 and WR21), $B - V$ colours when dereddened with $E(B - V) = A_V(\text{nebula})/3.1$ turned out to be bluer than -0.32 , the bluest $B - V$ colour of the Planck function, clearly indicating that the $A_V(\text{nebula})$ over-estimates the extinc-

¹ <http://www.inaoep.mx/~ydm/gtcmos/gtcmos.html>

Table 2. Sample of WR stars in M81.

ID (1)	R.A. (2)	Dec (3)	<i>V</i> (4)	<i>B</i> − <i>V</i> (5)	<i>B</i> − <i>I</i> (6)	<i>M</i> _{<i>V</i>0} (7)	Complex (8)	Size _{neb} (9)	<i>A</i> _{<i>V</i>} (10)
WR 1	9:55:01.663	+69:12:57.57	21.28	0.53	0.23	−6.72	Munch 18	100	0.2 (Neb)
WR 2	9:55:44.299	+69:07:19.43	20.53	−0.16	−0.25	−7.47	R06B06945	100	<0.5*
WR 3	9:55:16.651	+69:08:55.41	19.51	0.05	0.09	−8.49	kauf152	250	0.5 (Neb)
WR 4	9:55:35.890	+69:07:48.15	22.62	0.04	−1.05	−5.38	−	−	1.0 (Neb)
WR 5	9:55:09.785	+69:09:19.71	23.11	−0.23	−0.52	−4.89	−	−	1.5 (Neb)
WR 6	9:54:42.622	+69:03:42.67	21.56	−0.09	−0.22	−6.44	kauf125	20	0.2 (Gal)
WR 7	9:54:47.525	+69:04:34.22	20.45	0.16	0.37	−7.55	kauf127	80	0.8 (Neb)
WR 8	9:54:46.757	+69:04:22.51	21.43	0.05	0.11	−6.57	−	80	1.0 (Neb)
WR 9	9:54:42.566	+69:03:29.94	22.36	0.38	0.16	−5.64	kauf125	100	0.2 (Gal)
WR 10	9:54:49.418	+69:07:19.03	21.90	0.52	0.57	−6.10	kauf135	80	1.6 (Neb)
WR 11	9:54:48.643	+69:05:59.65	19.28	0.16	−0.16	−8.72	kauf128	80	0.2 (Gal)
WR 12	9:55:22.682	+69:09:52.26	21.79	0.35	0.20	−6.21	−	100	0.2 (Neb)
WR 13	9:55:24.986	+69:08:14.82	20.22	0.11	0.19	−7.78	kauf159	250	0.8 (Neb)
WR 14	9:55:16.488	+69:08:55.33	22.35	0.11	0.06	−5.65	kauf152	250	0.7 (Neb)
WR 15	9:55:28.817	+69:12:53.97	20.46	0.09	0.18	−7.54	Reg55	50	0.2 (Gal)
WR 16	9:56:16.831	+69:03:36.42	23.22	0.72	1.33	−4.78	Reg41	20	0.7 (Neb)
WR 17	9:55:47.042	+68:59:18.97	20.23	0.51	0.77	−7.77	kauf178	75	1.5 (Neb)
WR 18	9:56:06.300	+68:59:34.35	22.56	0.13	0.24	−5.44	kauf232	30	1.4 (Neb)
WR 19	9:56:05.225	+68:59:55.77	23.75	0.12	0.20	−4.25	Reg42	< 3	0.4 (Neb)
WR 20	9:56:00.211	+69:04:21.60	21.48	−0.04	−0.01	−6.52	Reg43	50	0.2 (Gal)
WR 21	9:56:17.969	+69:05:09.88	22.01	−0.04	−0.18	−5.99	−	< 3	<0.9*

Brief explanation of columns: (1) Name of WR star adopted in this study. Detections WR 1–WR 14 are from Paper I, whereas WR 15–WR 21 are new detections; (2–3) Right Ascension and declination in the FK5 system on the astrometrised *HST* image, where the M 81 nucleus is located at R.A.=148.88828° (9:55:33.188) and Dec=69.065263° (+69:03:54.95); (4–6) Apparent magnitude and colours in F435W(B), F606W(V) and F814W(I) bands; (7) Absolute magnitude in F606W band (*M*_{*V*0}) using a distance modulus of 27.80 mag, and Galactic extinction *A*_{*V*} = 0.20 mag (Schlafly & Finkbeiner 2011); (8) Star-forming complex from Pérez-González et al. (2006) embedding the WR star; (9) Size in parsec of the nebulosity around the WR star as measured on the F606W image; (10) Extinction *A*_{*V*} (mag). Asterisk(*) indicates an upper limit. See §2.4 for details.

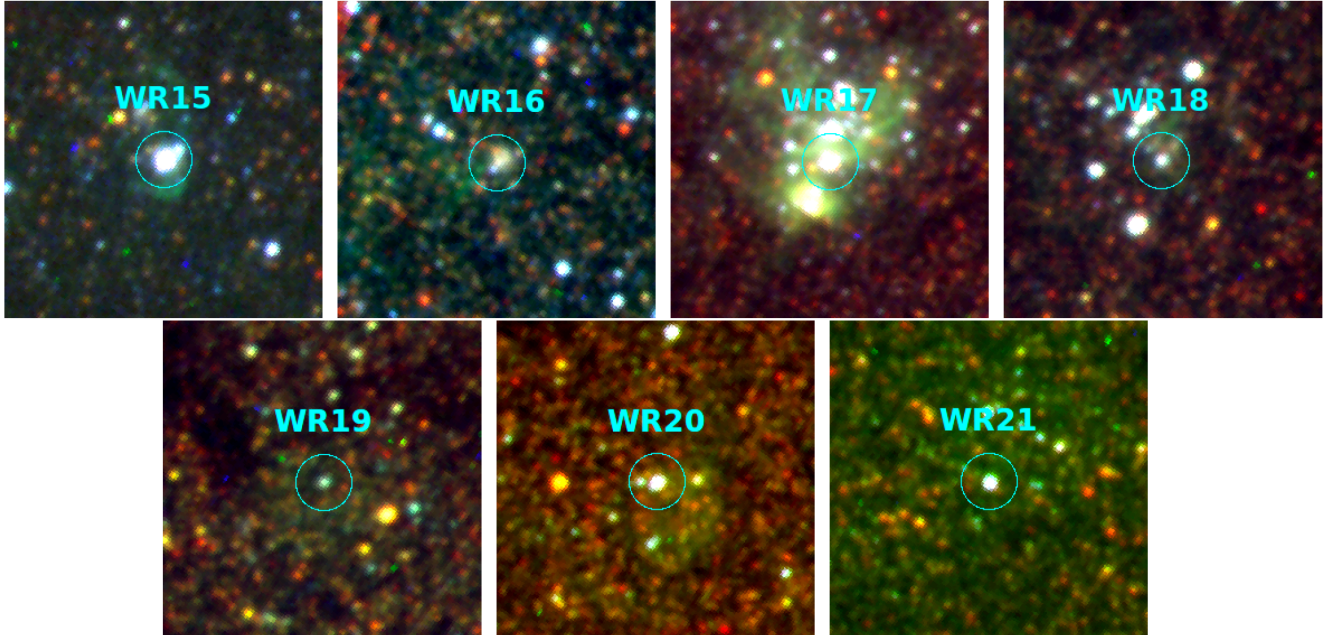


Figure 2. 100 pc×100 pc colour-composite *HST*/ACS cut-outs around the 7 new WR locations in M81 (WR 15–21). Red, green and blue correspond to the *HST*/ACS F814W, F606W and F435W filters, respectively. The WR stars are identified by circles of 1.0'' diameter, which is comparable to the slitwidth used in these observations. The F606W filter intercepts H α line, which gives a green appearance to the ionized nebulae and bubbles. North is up and east to the left in all images.

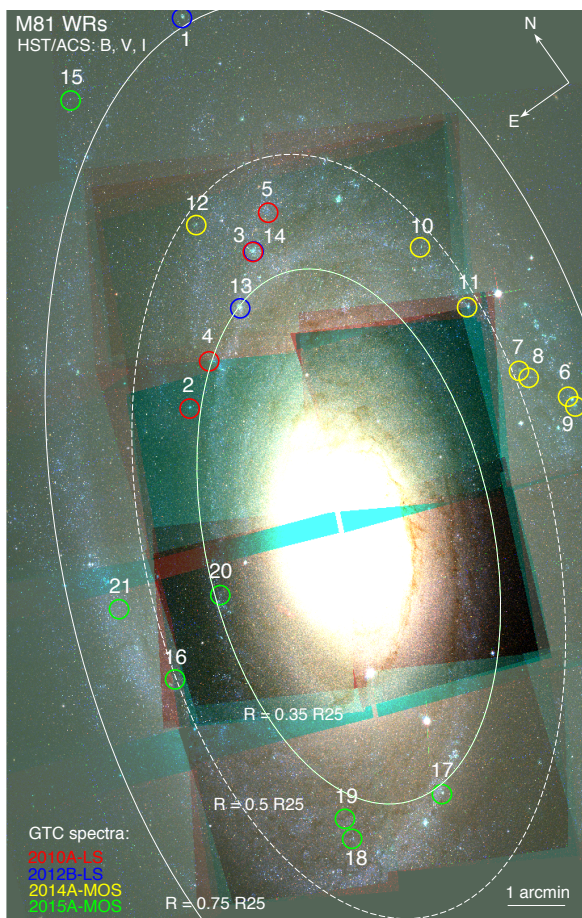


Figure 3. Colour-composite mosaic image of M81 using *HST* ACS images in the F814W (red), F606W (green) and F435W (blue) filters showing the 21 locations (circles) where WR features are detected in our GTC spectra spanning over 4 observing runs. Colours red, blue, yellow and green of the circles correspond to observing runs 2010A (longslit), 2012B (longslit), 2014A (MOS) and 2015A (MOS), respectively. The 7 new detections, labelled as WR15–WR21 in this work, are indicated with green circles. Different galactocentric distances are indicated with ellipses of semi-major axis = 0.35, 0.5 and 0.75 R_{25} .

tion towards these WR stars. For these cases, we give an upper limit calculated as $A_V = 3.1 \times (B - V + 0.32)$. Reduced extinction towards these WRs, as compared to the $A_V(\text{nebula})$, is not unexpected given that the strong winds emanating from the WR stars often create gas and dust-free zones in the immediate vicinity of the star. Thus, in general, $A_V(\text{nebula})$ is an upper limit to the extinction of the WR star. Hence, we dereddened all spectra with two limiting values of A_V : (1) maximum represented by $A_V(\text{nebula})$ and (2) minimum given by $A_V(\text{Gal}) = 0.20$. Both these dereddened spectra were analysed in §3.1 to determine its WR content.

3 CLASSIFICATION OF WR STARS

WR stars are identified and classified using the relative strengths of various transitions of nitrogen (N), carbon (C)

and oxygen (O) ions, in addition to that of doubly ionized helium (He II). Most of these transitions are located around two wavelengths, commonly known as the blue bump (BB; $\sim 4600\text{--}4700 \text{ \AA}$) and the red bump (RB; $\sim 5800\text{--}5840 \text{ \AA}$). The BB contains one or several He II, N III, N V and C IV lines, whereas the RB is made mainly of C IV lines. WR stars exhibiting any N line are classified as WN type, whereas those containing a C line are of WC type. Rarely a WR spectrum of a Galactic star contains both the N and C lines. These rare cases have been named as transitional WN/C sub-types (Conti & Massey 1989). Each sub-type is further classified into early (hereafter WNE and WCE) or late (hereafter WNL and WCL), depending on whether the detected features are of high or low ionization species, respectively. The emission lines of both the high and low ionization states of N are located in the BB and those of C in the RB, at separable wavelengths. Thus, the location of the bumps in the spectra allows the classification into early and late types. The He II line is seen in both the WN and WC types. Furthermore, in the WC phase, lines are systematically broader than in the WN type (Conti & Massey 1989). All these well-known characteristics make it possible to classify WR stars into its sub-types just by the analysis of their BB and RB (Smith 1968; Smith, Shara, & Moffat 1996; Crowther, De Marco, & Barlow 1998).

Unlike the Galactic WR stars, typical slitwidths used in spectroscopic observations intercept surrounding nebulae around extra-galactic WR stars. In addition, some of the ionic lines are faint to be detected at the distance of M81 even with the 10-m class telescopes. This inhibits a direct classification into WR subtypes from the observed spectra. This limitation is overcome by using the template spectra for classification of the observed extra-galactic WR spectra (e.g. Hadfield & Crowther 2006, 2007; Kehrig & Pérez-Montero 2013). The most commonly used templates for this purpose are from the observations of WR stars in the LMC. Comparison of the strengths of WR features in the template and observed spectra gives an indication of whether the observed feature belongs to an individual star or to multiple stars. We use the template fitting method to classify our WR spectra in M81, which is described below.

3.1 Template fitting of M81 spectra

Given that the metallicities obtained by direct method in M81 (Arellano-Córdova et al. 2016) compare well with that of the LMC, we use the LMC templates presented in Crowther & Hadfield (2006). These are available² for 4 sub-types of N-rich WRs: WN7-9, WN5-6, WN4-6 and WN2-4, and one sub-type of C-rich WRs: WC4. Class numbers greater than or equal to 6 are usually referred to as late and the rest being called as early. Thus, we have three WNL, and 1 WCE LMC templates. The template spectrum for each sub-type is an average of many stellar spectra of the same sub-types and are given in luminosity units. All the WRs in the LMC are at the same distance and hence the LMC templates are not affected by the errors in distance determination.

The template spectra were first scaled so that both the

² <http://www.pacrowther.staff.shef.ac.uk/science.html>

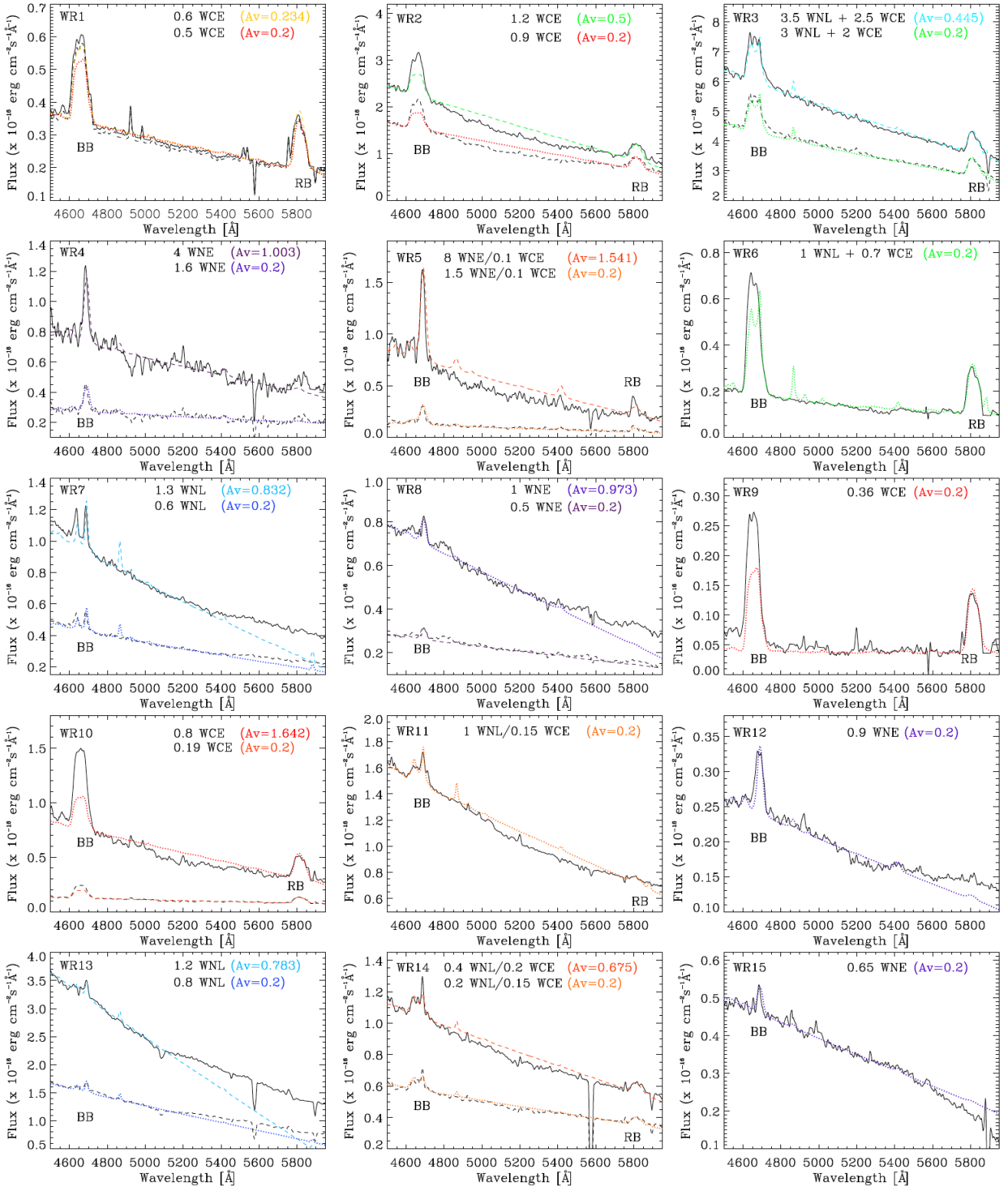


Figure 4. Observed spectra of 21 WR locations in M81 WRs (solid line), along with their best-fit LMC templates (coloured dotted line). WR name (WR 1–WR 21), name of the template (WNE, WNL, WCE) and the multiplicative factor required to match the observed bump strengths are indicated in each panel. Nebular spectra were subtracted for the first 15 using the spectra of pixels adjacent to the WRs, whereas such subtraction was not possible due to the short slitlengths for the last six spectra (for WR 16 – WR 21). Note that two values of A_V : (1) $A_V(\text{nebula})$ and (2) $A_V(\text{Gal}) = 0.20$ are considered in order to correct our spectra for dust extinction.

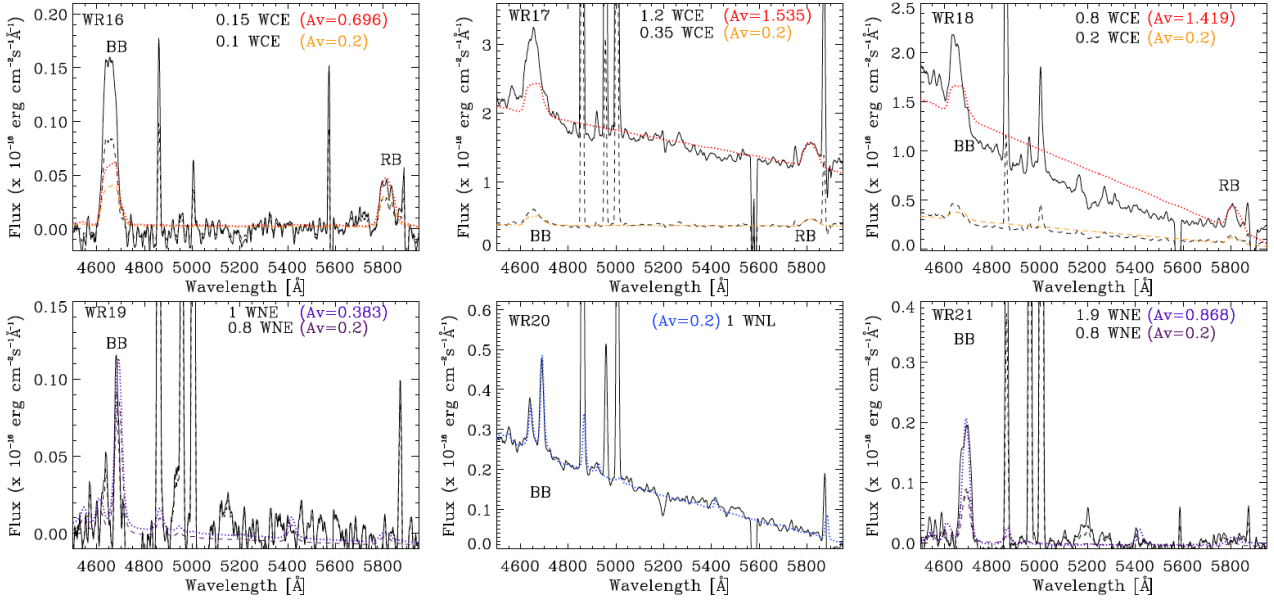


Fig. 4 continued.

observed and template spectra are in flux units at the distance of M81. We superposed the template spectrum of a given sub-type on an observed spectrum and visually examined the relative strengths of bumps in the two spectra. For a spectrum to be considered to belong to a candidate WC star, it should not only have a detectable RB, but also the sum of the luminosities of the two bumps should be at least 5×10^{35} erg s⁻¹. For these cases, we started with a template of WCE, and then applied a multiplicative factor on it so that the RB in the observed and template spectra are well matched. We then examined the BB. If the continuum levels at the BB are different, we added a pseudo-continuum (a straight line with a variable slope) to the template spectrum so that the observed and template spectra have the same slope between the bumps. If the observed BB shows an excess, especially on its bluer edge, it suggests the presence of a N line. We then found a multiplicative factor required to fit the BB, either with a WNL or a WNE template. The procedure is repeated until the observed bumps are well matched by a single, or a combination of templates. In cases where there is no detectable RB, or the sum of the bump luminosities is $< 5 \times 10^{35}$ erg s⁻¹, only the WNL and WNE templates are used.

The results of fitting LMC templates for our sample of 21 WR spectra, each dereddened using $A_V(\text{nebula})$ and $A_V(\text{Gal})$ and Cardelli et al. (1989) reddening curve are presented in Figure 4. The inferred WR type as well as the multiplicative factor (f_{WR}) that had to be applied to the template so that it matches the observed bump strengths for both the values A_V are indicated in each plot. As expected, dereddening increases the flux of the BB relative to that of the RB. Thus, f_{WR} is systematically higher for spectra dereddened with $A_V(\text{nebula})$ as compared to that with $A_V(\text{Gal})$. For WNL and WNE stars, the BB profile structure, as well as the observed intensities, are well-reproduced by the LMC templates. On the other hand, observed BB strength of M81 WCEs is systematically higher as compared

to that of the LMC WCE template, suggesting that this template is not adequate to the M81 WCEs.

The f_{WR} is directly related to the number of WR stars contributing to the analysed spectrum. The inferred number is often less than 1 even for spectra dereddened with $A_V(\text{nebula})$. This is expected as not all stars of the same sub-type have exactly the same bump strengths. In fact, there is almost an order of magnitude dispersion in the strength of the bumps within a given sub-type. These dispersions are tabulated for the LMC templates in Crowther & Hadfield (2006).

Given these relatively large intrinsic dispersions, and the possibility of WR stars experiencing lesser amount of extinction with respect to the surrounding nebula, we consider only those cases that required templates of two or more distinct WR subtypes as sure cases of multiple systems. For these reasons WR4 and WR21 are considered to be individual stars, in spite of having $f_{\text{WR}} > 1$ with $A_V(\text{nebula})$. The template used for both these cases is that of WN2–4. On the other hand, each of WR3 and WR6 required distinct templates (WNL and WCE), and hence are genuine multiple systems. The multiplicative factors using $A_V(\text{Gal})$, the inferred WR subtype, and the number of WR stars at each of our 21 locations are tabulated in Table 3.

There are only two compelling cases for the presence of multiple stars within our slits. These are the same two cases (WR3 and WR6) for which we have inferred the presence of multiple WR stars in Paper I, using the same LMC templates, but using observed spectra without dereddening corrections. We find 3 cases that show a weak RB, but with RB luminosity not exceeding 20% of the WCE template. The BB clearly suggests the presence of nitrogen features. We classify these 3 stars as transitional type (WN/C), following the definition of Conti & Massey (1989). Two of these transitional WRs (WR 11, WR 14) required WNL templates, while WR 5, required WNE template. Accordingly, we name them WNL/CEs and WNE/CEs, respectively. Red bump strength of these stars is lower than that of the LMC tran-

Table 3. Classification of WR stars with LMC templates.

ID (1)	$f_{\text{WR}} \times \text{Template}$ (2)	WR subtype (3)
WR 1	0.5 WC4	1 WCE
WR 2	0.9 WC4	1 WCE
WR 3	3 WN7-9+2 WC4	3 WNL+2 WCE
WR 4	1.6 WN2-4	1 WNE
WR 5	1.5 WN2-4/0.1 WC4	1 WNE/CE
WR 6	1 WN7-9+0.7 WC4	1 WNL+1 WCE
WR 7	0.6 WN7-9	1 WNL
WR 8	0.5 WN2-4	1 WNE
WR 9	0.36 WC4	1 WCE
WR 10	0.19 WC4	1 WCE
WR 11	1 WN7-9/0.15 WC4	1 WNL/WCE
WR 12	0.9 WN2-4	1 WNE
WR 13	1.2 WN7-9	1 WNL
WR 14	0.2 WN7-9/0.15 WC4	1 WNL/WCE
New 7		
WR 15	0.65 WN2-4	1 WNE
WR 16	0.1 WC4	1 WCE
WR 17	0.35 WC4	1 WCE
WR 18	0.2 WC4	1 WCE
WR 19	0.8 WN2-4	1 WNE
WR 20	1 WN7-9	1 WNL
WR 21	0.8 WN2-4	1 WNE

(1) WR identification number; (2) Multiplicative factors for each template (observed spectra dereddened using $A_V = 0.20$ mag);
 (3) Classification using LMC templates; The number corresponds to the number of WRs of the given sub-type.

sitional star BAT99-36, but are stronger than the red bump strength sometimes seen in WN stars (e.g. BAT99-26 in the LMC; Breysacher et al. 1999).

In summary, 19 of our spectra suggest the presence of individual stars within our slit, with 3 WNLs (WR 7, WR 13 and WR 20), 6 WNEs (WR 4, WR 8, WR 12, WR 15, WR 19 and WR 21), 7 WCEs (WR 1, WR 2, WR 9, WR 10, WR 16, WR 17 and WR 18), and 3 WN/Cs (WR 5, WR 11 and WR 14). The remaining 2 cases contain multiple WR stars (WR3 and WR6). An inspection at the *HST* images suggests that the separation between these multiple stars should be less than the PSF of the ACS camera, which is 1.8 pc at the distance of M 81. In our analysis in Paper I, we had reported 4 transitional stars. We here note that two of those (WR 5, and WR 14) retain this classification, and two others (WR 9, and WR 10) are reclassified as WCEs, with our new analysis, where we have taken into account reddening of the observed spectra. Additionally, WR 11, which was classified as WNL, is now re-classified as WN/C.

4 ANALYSIS AND DISCUSSION

WR features, the BB and RB, are usually blends of several ionic transitions. The lines constituting the BB are resolved in some of our WN types. When a WC component is present the lines are usually broader than 20 \AA and the presence of the C III line in the BB often gives it a broad, unresolved appearance spanning wavelengths between ~ 4600 to 4700 \AA . On the other hand, the RB is always broad and consists of C III and C IV lines. In addition, the adjoining nebular lines

Table 4. Emission lines contributing to the WR features.

ID (1)		Ion (3)	λ_0 (4)	WN (5)	WC (6)	WO (7)		
BB				L	E	L	E	
1	WR	He II	4686	a	a	o	s	o
2	WR	N III	a)4634	o	n	n	n	n
		N III	b)4641	o	n	n	n	n
3	WR	N V	a)4603	n	w	n	n	n
		N V	b)4620	n	w	n	n	n
4	WR	C III	4647/66	n	n	o	o	o
5	WR	C IV	4658	n	n	o	o	a
6	Neb	He I	4713					
7	Neb	He II	4686					
RB								
8	WR	C III	5696	n	n	a	n	n
9	WR	C IV	5801/12	w	w	o	a	a
10	Neb	N II	5755					
11	Neb	He I	5876					
VB								
12	WR	O VI	3811/34	n	n	n	n	a

(1) Identification number of the Gaussian components in blue (BB), red (RB) and a 'violet' (VB: bluer) bumps. (2) Nature of the contributing emission line: WR (broad) or nebular (narrow); (3) The emitting ion; (4) Rest wavelength in \AA ; (5-7) WR subtype where the corresponding emission line appears: always seen (a), often seen (o), weak (w) or never seen (n), as for the information available at Smith (1968); Smith, Shara, & Moffat (1996); Crowther, De Marco, & Barlow (1998). Late and Early types for WN and WC are indicated by the column header letters L and E, respectively.

(He I λ 4713 in the BB; [N II] λ 5755 and He I λ 5876 in the RB) often blend into the bumps. In Table 4 we list all the lines, both from the WR atmosphere and the surrounding nebula, that contribute to the bumps.

The individual lines contributing to the bumps can be recovered by using multiple-component Gaussian fitting. The decomposition would not only allow us to check whether the recovered lines are consistent with its classification made through LMC template fitting, but also allow us to determine the line parameters such as flux and width. Hence, we carried out multi-component Gaussian analysis of bumps.

4.1 Bump luminosities of M 81 WRs

We carried out the multiple-component Gaussian analysis of all our WR spectra with a tailor-made code developed for that purpose which uses the IDL routine LMFIT³. The fittings were carried out on the spectra dereddened by $A_V(\text{Gal})$. We used the lines listed in Table 4 to define Gaussians centered at the rest wavelengths (λ_0) of individual transitions. The λ_0 values of the transitions were taken from the NIST atomic

³ The LMFIT function (lmfit.pro) performs a non-linear least squares fit to a function with an arbitrary number of parameters. It uses the Levenberg-Marquardt algorithm, incorporated in the routine *mrqmin* of Numerical Recipes in C: The Art of Scientific Computing (Second Edition), Cambridge University Press.

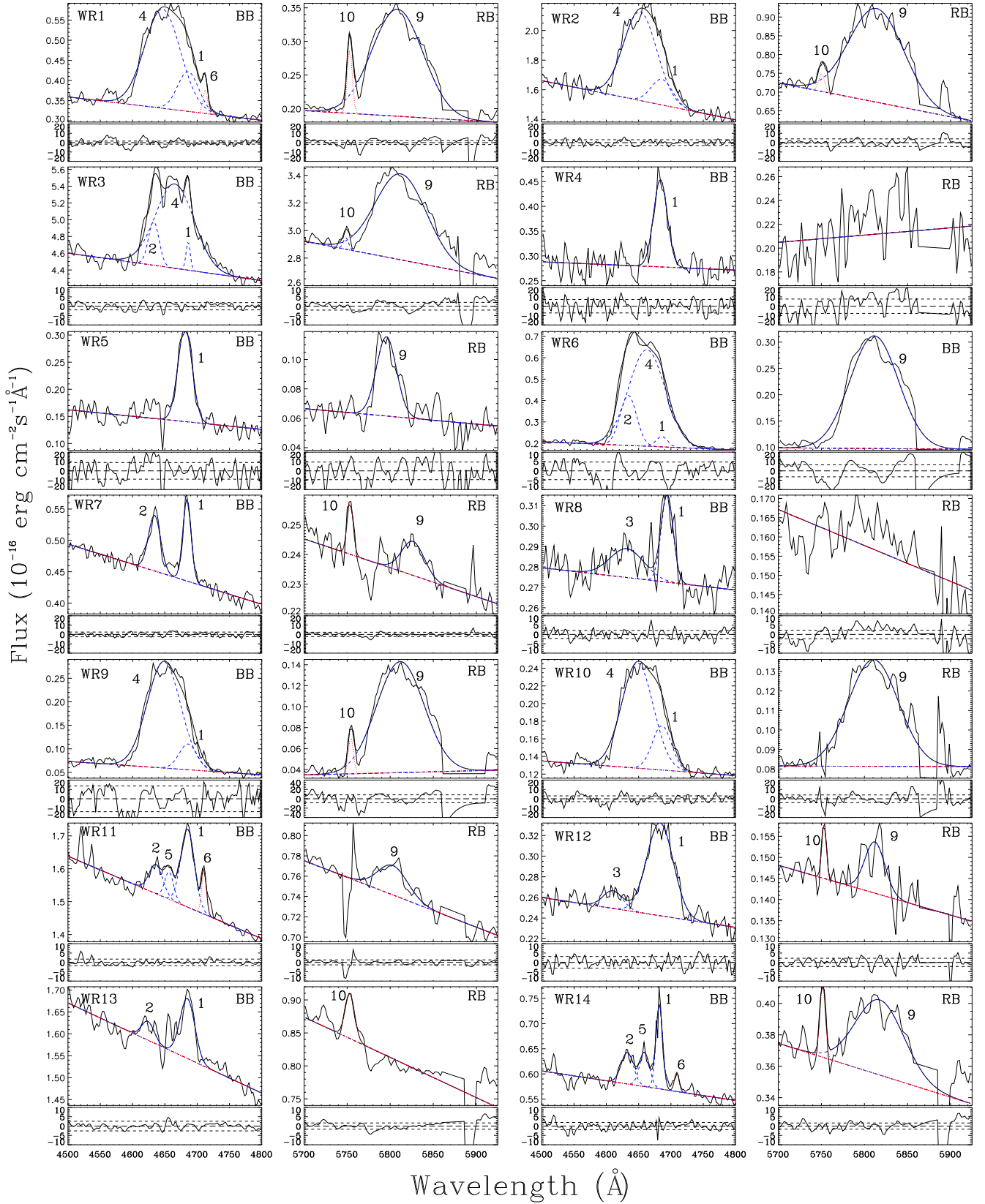


Figure 5. Multi-component Gaussian fits to the blue (*left*) and red (*right*) bumps: broad lines (dashed blue); nebular (dotted red when present); the sum (black). The fitted continuum is shown by the dashed straight line. The spectrum is identified by its WR number, and the fitted components are identified by the numbers 1–12 (see column 2 of Table 4). * indicates C III/C IV. Residuals are shown at the bottom of each panel.

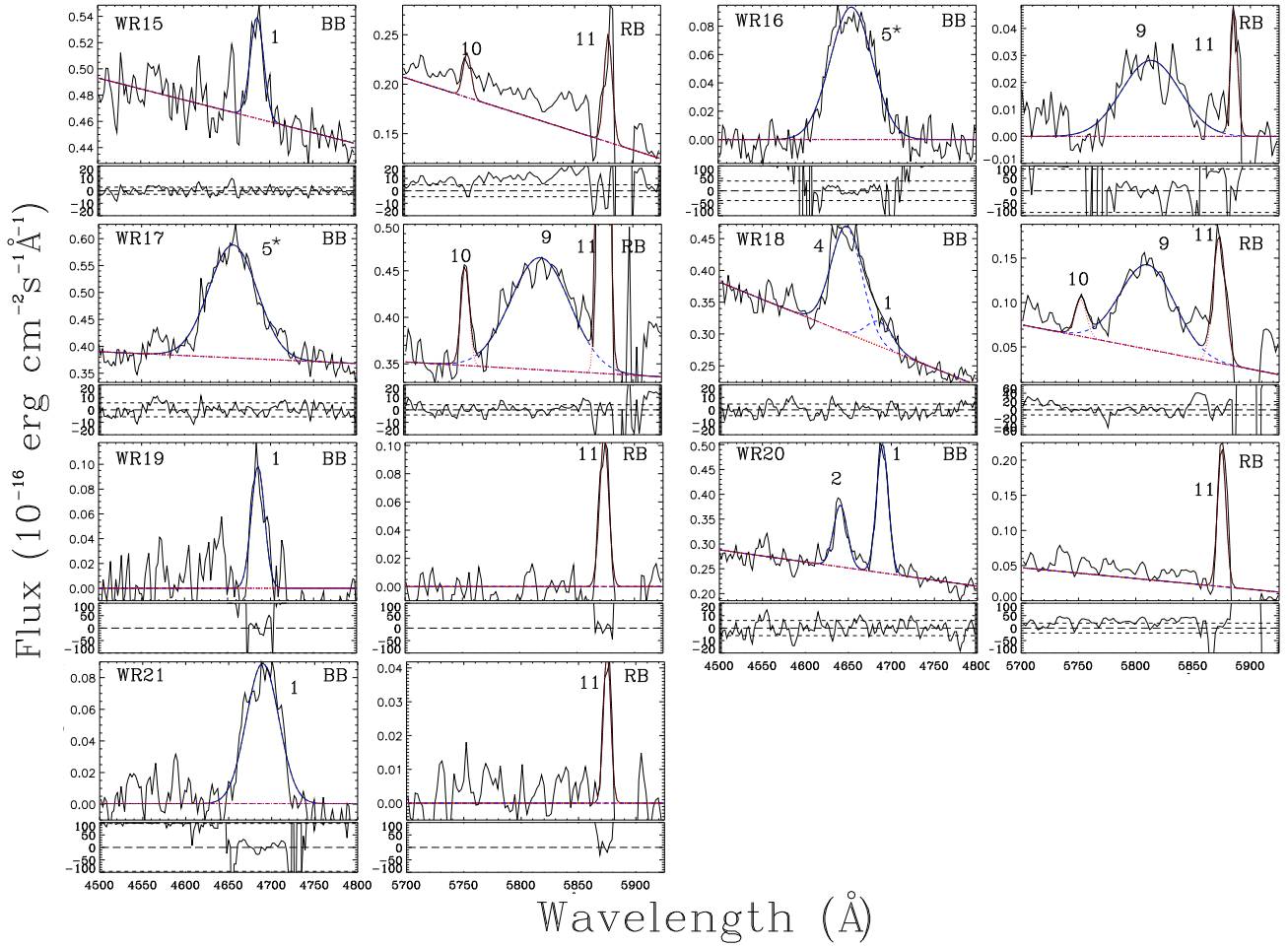


Fig. 5 continued.

spectra database⁴. For each bump, a continuum is defined by linearly interpolating on the red and blue sides of the bumps, avoiding any lines in these parts of the spectrum. Two of the 3 parameters, the peak intensity I_0 and the line width σ that defines each Gaussian, were left free. Any line with a full width at half maximum (FWHM) $> 9 \text{ \AA}$ (that is $\sigma > 4 \text{ \AA}$), which is the typical value for the instrumental profile, is defined as a broad line associated with a WR star. The third parameter, λ_0 , is fixed to one of the values listed in Table 4.

The fitting program is executed interactively, where the visually noticeable nebular lines were fitted first, using a Gaussian of FWHM $\sim 9 \text{ \AA}$, appropriate to the instrumental profile. For the BB, the He II broad component is fitted next. Residuals are examined for a peak near any of the other listed lines. If present, a second broad line is fitted and residuals were re-examined. While fitting this second line, the σ and I_0 of the first line were left free. The process of examining the residuals and adding a new line is continued until the residual is indistinguishable from the noise in the spectrum. In none of the cases, the RB required more than one broad component. In the iterative process, any faint nebular lines, if needed, were fitted.

The results of Gaussian fittings of WR spectra are shown in Figure 5. Structure of the BB is found to be complex, with a few objects fitted with a single Gaussian, while the majority required at least two Gaussians. For example, WR 5 shows the most simple case: a single Gaussian was needed; WR 7 shows the case where two Gaussians were needed which are easily identified as independent components, even by eye; WR 3 and WR 6 shows a BB without any noticeable peak, which is best fitted with 3 Gaussians, corresponding to N III, C III and He II lines. Given the limitations in obtaining unique values of the fitted Gaussian when more than 2 components are required, we fixed the FWHM of the C III line in the BB to the corresponding value for the C IV line in their RB. Other cases where more than 2 lines were required, individual lines are partially resolved and hence their FWHM parameters of the fit are left free.

Multi-Gaussian fittings to the BB and RB gave the luminosity, FWHM and Equivalent Width (EW) of all the fitted Gaussians for each WR source of the sample. The parameters of the broad He II $\lambda 4686$ line in the BB and the C IV $\lambda\lambda 5801/12$ line in the RB are tabulated in Table 5. Parameters for other broad lines in the BB are given in Table 6. Broad He II $\lambda 4686$ line is present in the BB in all but two cases. The two sources without the He II $\lambda 4686$ line are WR 16 and WR 17, where the BB is made up of

⁴ <http://physics.nist.gov/PhysRefData/ASD/>

the C III/C IV line. RB is detected in these two sources and hence they are clearly WC stars.

The recovered lines from Gaussian fittings for all sources are in agreement with the lines expected for their classification (see Table 4). For example all WNLs show a nitrogen line in the BB (in addition to the He II line) and WCs show one of the C lines (C III λ 4647/66 or C IV λ 4658) in the BB, in addition to the C IV $\lambda\lambda$ 5801/12 line in the RB. The recovered N line in all WNLs is the N III $\lambda\lambda$ 4634/41 line. All WNEs are not expected to show N lines, and when it is present it is usually the N V λ 4603/20 line. The only apparent exception is the WNE source WR8. We detect both the N and C lines in sources classified as transitional. In two of these transitional objects (WR 11 and WR 14), a C line is recovered in addition to the C IV $\lambda\lambda$ 5801/12 line in the RB. This further justifies the transitional nature of this component.

The resultant Gaussian fit to the He II λ 4686 line agrees with the rest wavelength of this line within $\sim 2 \text{ \AA}$ for all cases except WR 8, WR 20 and WR 21. Given that each spectrum was Doppler-corrected using the mean velocities of the nebular lines in the same spectrum, this agreement suggests that the relative radial velocity between the WR star and the surrounding ionized gas is less than 125 km s^{-1} . Dispersion in the central wavelength of the other components is larger, which is expected as several transitions at slightly different wavelengths contribute to these components.

The He II λ 4686 line is redshifted by 8 \AA in WR 8 and 4 \AA in WR 20 and WR 21 (see λ_0 in Table 5), suggesting that these objects are moving radially at velocities of 500 and 250 km s^{-1} , respectively, with respect to the surrounding ionized gas. The large Doppler velocity of WR 8, resolves the apparent inconsistency of the inferred N line for this WNE star. The recovered $\lambda_0 = 4632$ is closer to the N III $\lambda\lambda$ 4634/41 rather than the N V λ 4603/20 line. Taking into account its Doppler shift and the large FWHM of the Gaussian fit, the recovered N III line is consistent with the N V λ 4603/20 line, which is characteristic of WNE stars.

The trends of the relative strengths of the He, N and C lines for different spectroscopic WR sub-types are summarized in Figure 6. We sorted the WR sub-types following the sequence suggested by the single-star evolutionary models. Thus WNLs are to the left (shown by the blue hatches), followed by WNEs (green), transitional (magenta) and WCEs (red). Multiple stars are positioned at the extreme right. We choose the sum of the luminosities of blue and red bumps for normalizing the luminosities of individual transitions. In the upper panel we show this total luminosity (L_{tot}) as well as the BB luminosity for all our WR sources. WNL and WNE stars have only the BB and hence the two luminosities are the same. Within each sub-class, our WR stars are arranged in the increasing order of L_{tot} . A clear trend of increasing L_{tot} as a function of evolutionary stage can be seen. All spectra showing a RB have at least $L_{\text{tot}} = 4 \times 10^{35} \text{ erg s}^{-1}$. The remaining three panels show the luminosities of He II, N and C lines, all normalized to L_{tot} . From WNL to WNE, the N fraction decreases, and in WCEs, the He II is weak or absent. These trends are exactly as expected in the massive star evolutionary scenario of WRs. The transitional stars have properties intermediate to WN and WC stars.

In Paper I, we showed that a diagram involving RB luminosity vs BB luminosity is able to separate different WR

sub-types. This diagram has the potential to help classify extra-galactic WR stars, where it is often difficult to identify all key ionic transitions that are commonly used for classification of LMC WRs. Furthermore, it is a common practice to use a typical luminosity of $1.6 \times 10^{36} \text{ erg s}^{-1}$ for the BB to estimate the number of WRs in WR galaxies and other distant starburst systems (Schaerer & Vacca 1998). This typical luminosity is based on the WRs in the LMC and the Milky Way and needs to be verified in other extra-galactic systems. We use the M 81 WR data to discuss the luminosities of the blue and red bumps and their dependence on the WR sub-type.

The multi-Gaussian fitting has allowed us to decompose the bumps into their individual ionic transitions. The method also provided us luminosities in these individual ionic transitions, without the contamination of nebular lines. The BB could contain one or more of the following broad emission lines: He II λ 4686, N III $\lambda\lambda$ 4634/41, N V λ 4603/20, C III λ 4647/66 and C IV λ 4658. So we summed the recovered luminosities (see Table 5 and Table 6) of these lines to obtain the total BB luminosity. For the case of the RB, we only included the luminosity of C IV $\lambda\lambda$ 5801/12. In seven cases (WR 4, WR 8, WR 13, WR 15, WR 19, WR 20, WR 21), where no RB was detected, a $3\sigma_{\text{RB}}$ upper limit is used as the luminosity of the RB, where σ_{RB} was calculated assuming that the RB occupies ~ 40 pixels ($\sim 80 \text{ \AA}$; $\sigma_{\text{RB}} = \sqrt{40}\sigma$, where σ is the continuum rms/pixel close to the RB).

The summed luminosities of blue and red bumps are given in the last 2 columns of Table 5 and are plotted in Figure 7. The 7 WRs with only an upper limit for their RB luminosity are shown in the figure by a vertical arrow pointing downwards. For comparison we measured the bump luminosities from the LMC templates, which are also shown in Fig. 7. This RB vs BB luminosity diagram shows that the N-rich WR stars are located in the lower-left luminosity range, whereas the C-rich WR stars are located towards the upper-right region with higher luminosities. Transitional objects, those classified as WN/C, lie at intermediate values. Finally, multiple systems exhibit the highest luminosities in both the RB and BB. For all the LMC WNL templates, the BB luminosities are clustered around the often used value of $1.6 \times 10^{36} \text{ erg s}^{-1}$. On the other hand, the two M 81 WNLs have a value which is around half of that. The BB is systematically fainter for the M 81 WNEs, and lies between the values for WNEs of LMC templates. For WCE stars, there is a large dispersion in the RB and BB luminosities in M 81 as well as the two templates used. The observed luminosities for these stars in M 81 are in the same range as that for the templates.

Single star evolutionary models follow the scenario proposed by Conti (1976), wherein WR stars are evolutionary products of O-stars. As an O-star starts losing mass following the exhaustion of hydrogen (H) in its core, it starts revealing the products of CNO H-burning in its atmosphere. As a consequence the surface abundance of He, N, C and O start increasing, at the cost of H (Meynet & Maeder 2005). A post main-sequence O-star is considered to be a WR star when its surface abundance of H drops to $\sim 50\%$. The first phase of a WR is the WNL. When the He abundance reaches $\sim 78\%$, it is considered to be WNE and when C abundance is greater than $\sim 20\%$ it is considered a WC star. Thus, the evolutionary sequence followed by WRs is from WNL to WNE

Table 5. Parameters of He II and C IV line from multi-component Gaussian fitting ($A_V = 0.20$ mag extinction correction)

ID (1)	He II					C IV					L_{bumps}	
	λ_0 (2)	L (3)	FWHM (4)	EW (5)	S/N (6)	λ_0 (7)	$L_{n(RB)}$ (8)	FWHM (9)	EW (10)	S/N (11)	L_{BB} (12)	L_{RB} (13)
WR 1	4686	6.4	38.5	12.5	60.6	5808	0.56	69.9	62.8	48.5	33.3	18.7
WR 2	4686	11.3	39.0	4.8	32.3	5814	0.43	74.6	29.6	24.5	72.2	31.3
WR 3	4686	4.4	7.6	0.6	51.7	5812	0.58	70.0	16.7	48.9	126.9	73.3
WR 4	4684	7.4	25.0	16.9	14.0	–	0.06*	–	–	13.1	7.4	0.5*
WR 5	4681	7.5	25.6	33.9	11.2	5796	0.33	27.2	25.5	10.6	7.5	2.5
WR 6	4686	1.7	20.9	5.9	21.3	5811	0.37	66.2	154.1	15.5	63.5	23.8
WR 7	4684	3.3	15.1	4.8	39.7	5827	0.09	31.0	1.6	43.8	6.6	0.65
WR 8	4694	1.6	21.8	3.6	46.7	–	0.04*	–	–	44.0	3.0	0.1
WR 9	4686	3.0	32.7	34.1	7.3	5812	0.44	65.0	197.1	11.9	26.1	11.5
WR 10	4686	2.9	34.9	15.0	32.1	5810	0.44	68.5	49.1	24.1	14.5	6.3
WR 11	4685	9.9	24.8	4.2	56.9	5803	0.13	41.1	1.7	74.8	15.8	2.0
WR 12	4683	7.3	48.1	19.0	32.3	5812	0.07	27.3	2.5	45.8	8.3	0.6
WR 13	4685	6.2	26.7	2.5	38.7	–	0.06*	–	–	60.2	7.8	0.4*
WR 14	4682	3.4	12.0	3.8	51.6	5818	0.69	66.2	9.5	60.5	7.8	5.3
WR 15	4685	2.4	18.3	3.3	34.6	–	0.14*	–	–	20.8	2.4	0.3*
WR 16	–	–	–	–	2.5	5813	0.31	59.5	–	1.2	9.0	2.8
WR 17	–	–	–	–	17.8	5819	0.53	61.0	22.8	24.3	23.3	12.3
WR 18	4686	2.3	35.6	5.2	21.4	5810	0.63	55.8	120.2	8.2	14.1	8.9
WR 19	4685	3.0	18.2	–	1.0	–	0.07*	–	–	0.9	3.0	0.2*
WR 20	4690	6.9	15.9	18.2	16.4	–	0.03*	–	–	5.0	10.9	0.3*
WR 21	4690	6.6	44.6	–	1.0	–	0.02*	–	–	0.6	6.6	0.1*

(1) WR identification; (2) Observed center wavelength of He II λ 4686 [Å]; (3) Luminosity [1.0×10^{35} erg s $^{-1}$]; (4) Full Width at Half Maximum (FWHM) [Å]; (5) Equivalent Width (EW) [Å]; (6) Continuum Signal to Noise Ratio (S/N) at 4750–4830 Å; (7) Center of C IV $\lambda\lambda$ 5801/12 feature; (8) C IV $\lambda\lambda$ 5801/12 luminosity normalized to L_{BB} ; (9) FWHM [Å]; (10) EW [Å]; (11) S/N at 5600–5730 Å. (12) BB luminosity (L_{BB}) [1.0×10^{35} erg s $^{-1}$]; (13) RB luminosity (L_{RB}) [1.0×10^{35} erg s $^{-1}$]. * indicates 3σ upper limits.

Table 6. Parameters of the 2nd and 3rd Gaussian components ($A_V = 0.20$ mag extinction correction).

ID (1)	N III–N V				C III–C IV			
	λ_0 (2)	L_n (3)	FWHM (4)	EW (5)	λ_0 (6)	L_n (7)	FWHM (8)	EW (9)
WR 1	–	–	–	–	4646	0.81	65.1	51.6
WR 2	–	–	–	–	4652	0.84	60.5	25.3
WR 3	4633	0.03	19.3	0.6	4665	0.93	70.0	17.0
WR 4	–	–	–	–	–	–	–	–
WR 5	–	–	–	–	–	–	–	–
WR 6	4634	0.19	30.0	39.3	4663	0.79	66.2	170.3
WR 7	4634	0.50	22.3	4.7	–	–	–	–
WR 8	4632	0.48	61.5	3.4	–	–	–	–
WR 9	–	–	–	–	4649	0.89	60.9	247.4
WR 10	–	–	–	–	4648	0.80	57.6	57.7
WR 11	4636	0.23	24.6	1.5	4657	0.14	15.8	0.9
WR 12	4610	0.12	35.6	2.6	–	–	–	–
WR 13	4624	0.21	22.9	0.7	–	–	–	–
WR 14	4632	0.30	22.1	2.5	4659	0.26	17.8	2.2
WR 15	–	–	–	–	–	–	–	–
WR 16	–	–	–	–	4655	1.00	57.3	–
WR 17	–	–	–	–	4656	1.00	66.1	39.0
WR 18	–	–	–	–	4648	0.84	42.1	25.0
WR 19	–	–	–	–	–	–	–	–
WR 20	4641	0.36	18.7	9.8	–	–	–	–
WR 21	–	–	–	–	–	–	–	–

(1) WR ID; (2) Observed center wavelength of N III $\lambda\lambda$ 4634/41 or N V λ 4603/20 [Å]; (3) $L_{NIII-NV}$ normalized to L_{BB} ; (4) FWHM [Å]; (5) EW [Å]; (6) Observed center wavelength of C III/C IV [Å]; (7) $L_{CIII-CIV}$ normalized to L_{BB} ; (8) FWHM [Å]; (9) EW [Å].

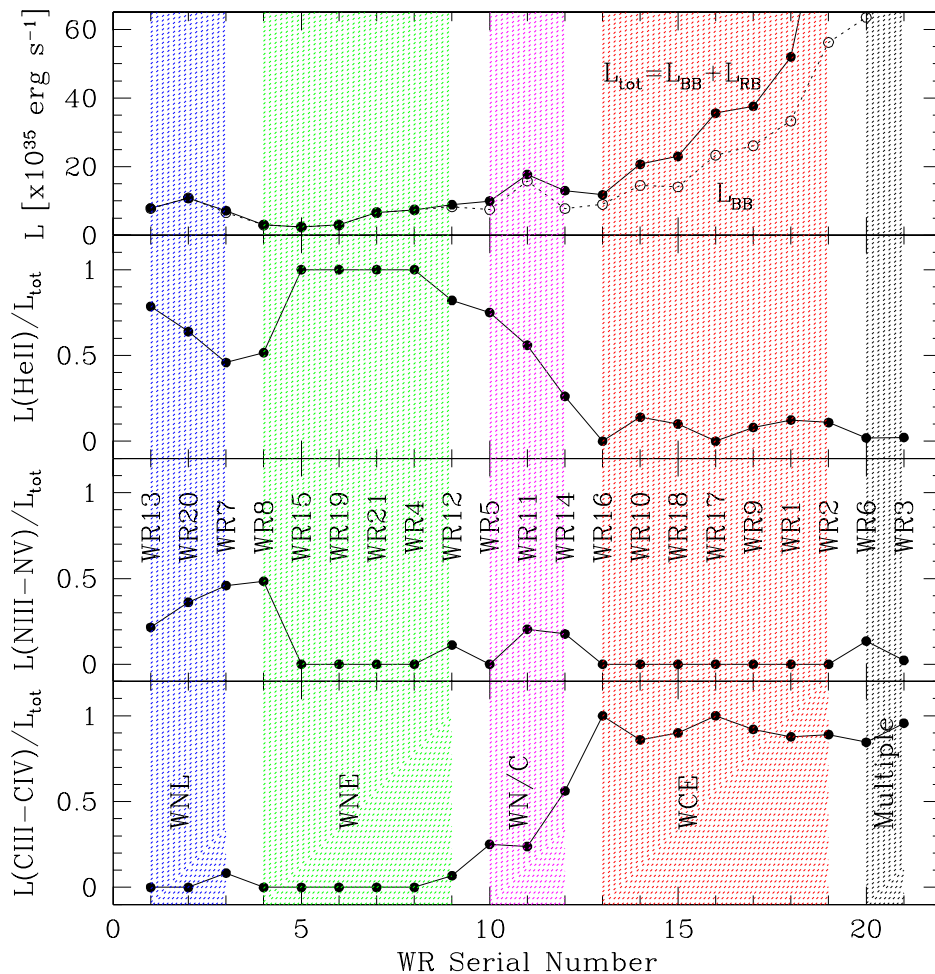


Figure 6. Gaussian-decomposed luminosities of He, N, and C ions as a function of WR sub-type for the 21 M81 WRs, which are grouped into WNL (blue), WNE (green), transitional (magenta), WCE (red) subtypes. Locations with multiple WRs are shown by the black hatched area to the right. Individual WRs are identified in the second panel from the bottom. Top panel shows the summed luminosity (L_{tot}) of the two bumps (solid circles and lines) and the blue bump luminosity (dotted line joining empty circles). The next 3 panels show luminosities of He, N and C lines, all normalized to L_{tot} .

to WCs. We show this trajectory in Figure 7 by arrowed curves. The transitional WN/C stars lie in this trajectory intermediate to WNE and WC stars.

In single star evolutionary models without rotation, the surface N abundance drops to zero at the onset of the WC phase, and C abundance is zero in the WN phase. In this scheme, a star is not expected to simultaneously show N and C lines, and hence these models cannot explain the transitional WN/C stars. Meynet & Maeder (2005) found that stars rotating at initial speeds of $\sim 300 \text{ km s}^{-1}$ were able to bring out the He-burning products from its core before removing completely the CNO-enriched envelope of stars with masses between $\sim 30\text{--}60 M_{\odot}$. Hence, these stars evolve through the transitional WN/C phase for a non-negligible duration, during which time they show the broad lines of both N and C simultaneously. The location of our WN/C stars along the evolutionary path between the WNE and WC phase is consistent with this scenario.

The relative locations of different sub-types follow the same trend in LMC and M81. As discussed above these

trends are consistent with the sequence of occurrence of different sub-types in current single star evolutionary models. M81 is a star-forming galaxy, with a few hundreds of WRs expected in it and hence future searches would increase the sample size. Nevertheless, we deem it relevant to carry out a deeper analysis of our present dataset that would enable us to make quantitative comparisons with the WRs in other galaxies. The characteristics of our transitional WN/C stars resemble those of the WN subtypes in the BB, and those of the WC subtypes in the RB. In addition, the RB fluxes of our WN/C are lower than those of the WCE stars. Therefore, a multiple WN + WC system in which the BB would dominate the flux and shape of a WC is discarded.

A WR detection in an extragalactic spectrum may contain contribution of more than one star within the observed slit, either because they are in a binary or they are part of a cluster. If the two stars are of the same type (WN or WC), the combined spectrum would be a simple multiplication of the spectrum of that type. However, if the two stars are of different types, the combined spectrum will contain both

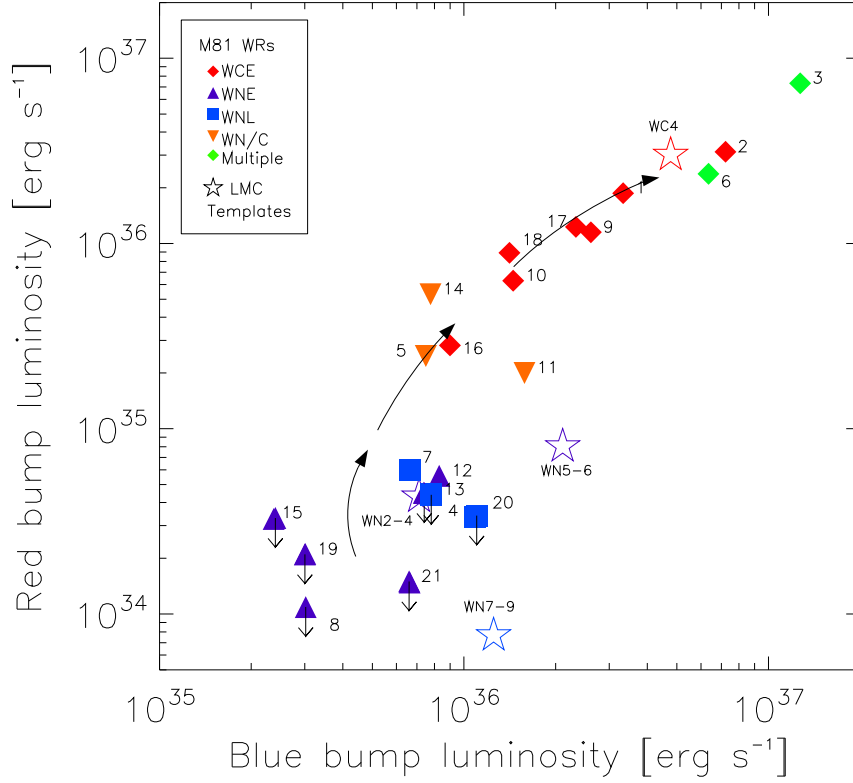


Figure 7. RB vs BB luminosity diagram for the 21 WR stars in M81. A 3σ upper limit is indicated where no RB was detected. Their spectral identification is indicated, as well as their classification using observational templates of individual WR stars in the LMC: WNL (blue box), WNE (purple triangle), WCE (red diamond), transitional WN/C (orange inverted triangle) and multiple stars (green diamond). LMC observational templates from different WR-types are shown overplotted with filled and empty stars. Arrows indicate the expected trajectory of single star evolutionary models in this diagram.

the N and C lines. Spectra of such multiple systems can also mimic the spectra of rarely seen transitional WN/C type. However, a detailed analysis of the spectra can distinguish between these possibilities. The spectra of three of our objects (WR 5, WR 11 and WR 14) are classified as transitional WR stars: these objects clearly show a residual indicating the need for a nitrogen line, when using only a carbon-rich template and vice versa. The requirement for a WCE in these stars are guided by the presence of RB in them. The strength of carbon line in the RB in these 3 stars is much weaker as compared to that of a typical WCE and hence are unlikely to be multiple systems. Multi-Gaussian fitting suggests the presence of a C line in the BBs of WR 11 and WR 14. This reinforces the need for a WC component. The observed BB of WR 11 and WR 14, could only be fitted by having both WN and WC features. Specifically, without a WN feature there is a systematic residual at the blue edge of the BB. Although the BB of WR 5 looks like WN sub-type, the observed RB could only be produced by having also a WC feature.

5 SUMMARY AND CONCLUDING REMARKS

In this work, we reported the detection of WR features at 7 new locations in the nearby spiral galaxy M81. These detections were the result of spectroscopic observations of

the central stars of *HST*-detected ionized bubbles using the GTC/OSIRIS spectrograph at the 10.4-m GTC. Using the same instrumental set-up, we had earlier detected 14 locations with WR features in this galaxy. We carried out a detailed analysis of all the 21 WR spectra using the well-established LMC templates of WRs of different spectroscopic sub-types with the intention of classifying and quantifying the WR responsible for the observed bump strength.

In general, the bump strengths do not require more than one WR star in 19 cases of which 3 are WNLs (WR 7, WR 13 and WR 20), 6 WNEs (WR 4, WR 8, WR 12, WR 15, WR 19 and WR 20), 7 WCEs (WR 1, WR 2, WR 9, WR 10, WR 16, WR 17 and WR 18), and 3 WN/Cs (WR 5, WR 11 and WR 14). The remaining 2 cases contain multiple WR stars (WR 3 and WR 6). Examination of the *HST* images suggests that the separation between these multiple stars is less than the PSF of the ACS camera, which is 1.8 pc at the distance of M81. None of the detections correspond to WCL and WO types. One of the detected WRs (WR 8) is found to have high (500 km s^{-1}) radial velocity with respect to the surrounding ionized gas.

We analysed the observed bumps using multiple-component Gaussian fitting in order to recover the ionic transitions responsible for the bumps. In all cases, the recovered ions are consistent with those expected for the inferred sub-type using the templates. All WRs of a given sub-type occupy a distinct zone in the RB vs BB luminosity diagram,

with our transitional objects having bump luminosities intermediate between that of WNs and WCs. The BB luminosity of M 81 WNs is at least a factor of 2 less than the often used typical value of 1.6×10^{36} ergs $^{-1}$ based on the LMC WNs. No such difference is found for WC stars. We suggest that RB vs BB diagram is a straightforward tool of spectral classification of WR stars, especially for extragalactic sources (single or in clusters) where detailed spectra from each star cannot be obtained.

The detection of as much as 19 individual WR stars in M 81, which is at a distance of 3.6 Mpc, opens up a new environment for testing the massive star evolutionary models.

ACKNOWLEDGEMENTS

The authors thank the referee Paul Crowther for his enlightening comments and suggestions improving this work. To Antonio Cabrera and the rest of the GTC staff for their help in carrying out the observations presented in this work and also the support during data reductions. This work is based on observations made with the NASA/ESA Hubble Space Telescope, obtained from the data archive at the Space Telescope Science Institute. STScI is operated by the Association of Universities for Research in Astronomy, Inc. under NASA contract NAS 5-26555. YDM thanks CONACyT for the research grant CB-A1-S-25070 and DRG for the research grant CB-A1-S-22784. VMAGG thanks to CONACyT, INAOE and UNACH, for the different supports to carry out this work. JAT and VMAGG are funded by UNAM DGAPA PAPIIT project IA100318.

REFERENCES

- Arellano-Córdova, K. Z., Rodríguez, M., Mayya, Y. D., & Rosa-González, D. 2016, *MNRAS*, 455, 2627-2643
- Breysacher, J., Azzopardi, M., & Testor, G. 1999, *A&AS*, 137, 117B
- Cardelli, J. A. A., Clayton, G. C., Mathis, J. S. 1989, *ApJ*, 345, 245
- Cabrera-Lavers, A. 2016, *ASP Conf. Ser.*, 507, 185
- Chen, Y., Bressan, A., Girardi, L., Marigo, P., Kong, X., & Lanza, A. 2015, *MNRAS*, 452, 1068-1080
- Chu, Y.-H., Treffers, R. R., & Kwitter, K. B. 1983, *ApJS*, 53, 937
- Conti, P.S., 1976, *Proc. 20th Colloqu. Int. Astrophysics.*, Liege, p. 193
- Conti, P. S., & Massey, P. 1989, *ApJ*, 337, 251-271
- Crowther P. A., De Marco O., Barlow M. J., 1998, *MNRAS*, 296, 367
- Crowther, P. A. 2007, *ARA&A*, 45, 177
- Crowther, P. A., & Hadfield, L. J. 2006, *A&A*, 449, 711
- Eldridge, J. J., Stanway, E. R., Xiao, L., McClelland, L. A. S., Taylor, G., Ng, M., Greis, S. M. L., Bray, J. C. 2017, *Publ. Astron. Soc. Australia*, 34, e058
- Freedman, W. L., Hughes, S. M., & Madore, B. F., et al. 1994, *ApJ*, 427, 628
- García-Segura, G., Langer, N., & Mac Low, M.-M. 1996, *A&A*, 316, 133
- Gómez-González, V. M. A., Mayya, Y. D., & Rosa-González, D. 2016, *MNRAS*, 460, 1555 (Paper I)
- Gruendl, R. A., Chu, Y.-H., Dunne, B. C., & Points, S. D. 2000, *AJ*, 120, 2670
- Hadfield, L. J., & Crowther, P. A. 2007, *MNRAS*, 381, 418
- Hadfield, L. J., & Crowther, P. A. 2006, *MNRAS*, 368, 1822-1832
- Hainich, R., Pasemann, D., & Todt, H., et al. 2015, *A&A*, 581, A21
- Hainich, R., Rühling, U., & Todt, H., et al. 2014, *A&A*, 565, A27
- Hamann, W.-R., Gräfener, G., & Liermann, A. 2006, *A&A*, 457, 1015
- Humphreys, R. M., Stangl, S., Gordon, M. S., Davidson, K., & Grammer, S. H. 2019, *AJ*, 157, 22
- Kehrig, C., Pérez-Montero, E., Vílchez, J. M., Brinchmann, J., Kunth, D., García-Benito, R., Crowther, P. A., Hernández-Fernández, J., Durret, F., Contini, T., Fernández-Martín, A., & James, B. L. 2013, *MNRAS*, 432, 2731-2745
- Kudritzki, R.-P., Urbaneja, M. A., Gazak, Z., Bresolin, F., Przybilla, N., Gieren, W., & Pietrzyński, G. 2012, *ApJ*, 747, 15
- Meynet, G., & Maeder, A. 2005, *A&A*, 429, 581-598
- Moffat, A. F. J. 2015, 2015wrs.conf, 13M
- Neugent, K. F., & Massey, P. 2011, *ApJ*, 733, 123
- Neugent, K. F., Massey, P. & Georgy, C. 2012, *ApJ*, 759, 11
- Osterbrock, D. E., & Ferland, G. J. 2006, *Astrophysics of gaseous nebulae and active galactic nuclei*
- Patterson, M. T., Walterbos, R. A. M., Kennicutt, R. C., Chiappini, C., & Thilker, D. A. 2012, *MNRAS*, 422, 401
- Pérez-González, P. G., Kennicutt, Jr., R. C., Gordon, K. D., Misselt, K. A., Gil de Paz, A., Engelbracht, C. W., Rieke, G. H., Bendo, G. J., Bianchi, L., Boissier, S., Calzetti, D., Dale, D. A., Draine, B. T., Jarrett, T. H., Hollenbach, D., & Prescott, M. K. M. 2006, *ApJ*, 648, 103
- Rosslowe, C. K. & Crowther, P. A. 2015, *MNRAS*, 447, 2322-2347
- Schild, H., Crowther, P. A., Abbott, J. B., & Schmutz, W. 2003, *A&A*, 397, 859
- Schaerer, D. & Vacca, W. D. 1998, *ApJ*, 497, 618
- Schlafly, E. F., & Esteban, D. P. 2011, *ApJ*, 737, 103
- Sell, P. H., Pooley, & D., Zezas, A., et al. 2011, *ApJ*, 735, 26
- Shenar, T., Hainich, R., & Todt, H., et al. 2016, *A&A*, 591, A22
- Smith, L. F. 1968, *MNRAS*, 138, 109
- Smith L. J., Crowther P. A., Prinja R. K., 1994, *A&A*, 281, 833
- Smith L. F., Shara M. M., Moffat A. F. J., 1996, *MNRAS*, 281, 163
- Toalá, J. A., & Arthur, S. J. 2011, *ApJ*, 737, 100
- van der Hucht, K.A. 2001, *New Astronomy Reviews* 45, 135
- Vink, J. S., Gräfener, G., & Harries, T. J. 2011, *A&A*, 536, L10